

On performance of thin-film meso-structured perovskite solar cell through experimental analysis and device simulation

F. Bonnín-Ripoll¹, Ya. B. Martynov², R. G. Nazmitdinov ^{3,4}, K.

Tabah⁵, C. Pereyra⁵, M. Lira-Cantú⁵, G. Cardona⁶, and R. Pujol-Nadal¹

¹Departament d'Enginyeria Industrial i Construcció,

Universitat de les Illes Balears, E-07122 Palma, Spain.

²State Scientific-Production Enterprise "Istok" Fryazino, Russia.

³Bogoliubov Laboratory of Theoretical Physics, Joint Institute for Nuclear Research, 141980 Dubna, Russia.

⁴Dubna State University, 141982 Dubna, Moscow region, Russia.

⁵Catalan Institute of Nanoscience and Nanotechnology (ICN2),

CSIC and the Barcelona Institute of Science and Technology (BIST),

Building ICN2, Campus UAB, E-08193 Bellaterra, Barcelona, Spain. and

⁶Departament de Matemàtiques, Universitat de les Illes Balears, E-07122 Palma, Spain.

In the last few years there is an unprecedented progress in the increase of the power conversion efficiency of perovskite solar cells. Evidently, further advances of the efficiency of these devices will depend on the constraints imposed by the optical and electronic properties of their constituents. Quite apparently that during the manufacturing process of a solar cell, there is an inevitable variation in the thicknesses of various functional layers, which affects the optoelectronic characteristics of the final sample. In this work a possible strategy of the analysis of the solar cell performance is suggested, based on statistically averaging procedure of experimental data. We present a case study, in which the optoelectronic properties of the meso-structured perovskite solar cell (with a mesoporous TiO_2 layer) are analysed within the method providing a deeper understanding of the device operation. This method enables an assessment of the overall quality of the device, pointing pathways towards the maximum efficiency design of a perovskite solar cell by material properties tuning.

Keywords: mesoporous, optoelectronic measurements and analysis, ray tracing, transfer matrix method, transport equations, power conversion efficiency

I. INTRODUCTION

Nowadays organic-inorganic halide perovskites, as solar cell light-absorbers, attract substantial attention. Solar cells with such photoactive layers are considered as one of the most promising competitors to silicon-based photovoltaics, reaching efficiencies of 25.8% only in two decades of development [1]. Low-cost production of these materials with high power conversion efficiency (PCE) pledge fast development of flexible solar cells [2]. Moreover, there is challenging future in improvement of their performance in order to reach their maximum efficiency (cf.[3]) by means: engineering of perovskite composition [4] or/and perovskite solar cell (PSC) constituents [5–9]; study and improvement of perovskite stability [10]; altering characteristics of optoelectronic behavior of PSC constituents [11] by incorporation, for example, light trapping mechanisms [12]; to name just a few.

Evidently, for further efficiency improvements of PSCs, the analysis of optical and electric properties of different layers in the device architecture is pivotal for optimizing light-harvesting in the absorber, whilst allowing coherent effects and parasitic absorption to be accounted in the stack design. In addition, this analysis should be based on statistically reliable estimates of noticeable dispersion

of various sample parameters during the manufacturing process. Partially, some attempts in this direction have been done in [13–15], where various type of simulations of optoelectronic properties of PSCs have been conducted recently. It is worth noting that for the analysis of optical properties various research groups (see, for example, [16–20]) use the software SCAPS-1D [21] as a main tool. This code does not, however, consider interference, scattering, or intermediate reflectors (see details in [21]), thus preventing the comprehensive analysis of the antireflection layer's interference and the influence of thin films thicknesses.

Also, a broad range of electron (hole) transport materials and back metal contacts have been considered to examine the performance of lead-free PSCs in [22]. It also became common to introduce a mesoporous TiO_2 layer between TiO_2 electron collecting contact and perovskite (the main absorber layer). This process decreases defect density at the absorber boundary, while may introduce additional resistance. Nevertheless, the effect of a mesoporous TiO_2 layer and its influence on the PSC performance remains in infancy. Here, we employ a ray tracing-based optoelectronic computational model [23] to reproduce the behaviour of a perovskite solar cell with a mesoporous TiO_2 layer and characterize experimen-

tal PSC samples. To this aim we further developed this model, incorporating a few novel elements to treat properly thin-film meso-structured perovskite solar cells.

The experimental device configuration (see Fig.1) is selected as the well established experimentally perovskite solar cell [24]. The measurements of optical transmittance have been performed in each stage of the manufacturing process. In this n-i-p junction device structure, apart the complex glass substrate, a thin and compact TiO_2 (c- TiO_2) is manufactured as an electron selective contact to facilitate the collection of photogenerated electrons from perovskite absorber. Next, to improve the efficiency of carrier collection a mesoporous TiO_2 (mp- TiO_2) is introduced to provide a suitable perovskite deposition [25]. In addition, the partial infiltration of halide perovskite into the mp- TiO_2 layer facilitates higher quantum yield for photo-excited charge separation. Spiro-OMeTAD has been utilized in establishing a good p-contact between the gold (Au) counter electrode with a perovskite absorber in our stack design. As mentioned above, we will elaborate the model [23] and discuss in detail the effective medium approach for analysis of the optical behaviour of mp- TiO_2 . Our approach is experimentally verified with measurements of the device reflection and transmission spectra. These characteristics have been measured by means of spectrophotometry techniques applied at each manufacturing stage. Finally, we make use of our approach to evaluate the dependence of the PSC performance on the properties of the mesoporous structure of the considered solar cell architecture, based on statistically averaged physical and geometrical parameters of the device.

II. METHODOLOGY

A. Device Characteristics

Since electronic and optical measurements cannot be performed on the same PSC sample, we use two batches of 24 solar cells, manufactured at the same conditions. One batch is used for optical measurements with interruptions on each phase of the process, while the second one is used for J-V characteristic measurements without any interruptions on each phase of the process.

Considering the deposition of a material as a new phase of the process, we have performed the measurements of optical transmittance of each PSC layer in each stage of the manufacturing process (see details in Appendix A). Stage 1 of the manufacturing process consists of the glass substrate, assuming the material as a multilayer system itself, formed by sodalime glass, SnO_2 , SiO_2 and fluorine doped tin oxide (FTO). In the stage 2 a layer of c- TiO_2 of the order of tens of nanometers is added by the spray pyrolysis technique. Next, a mp- TiO_2 layer is deposited in stage 3, followed by the subsequent deposition of a perovskite (stage 4) and Spiro-OMeTAD (stage 5), the latter three using the spin coating technique.

Next, using a solar simulator, the J-V characteristics of the PSCs in operation a second batch of 24 solar cells has been measured. The result of this measurements provides the average value of the short-circuit current $J_{sc} = 20.07 \text{ mA/cm}^2$ with a standard deviation 0.99 mA/cm^2 at irradiance 1000 W/m^2 . In this study we will focus on reproducing the behaviour of the reverse scan of the J-V characteristics. The scanning process conditions are discussed in [24].

B. Optoelectronic Model

To analyse the amount of transmitted, absorbed and reflected light in each of the materials present in the PSCs, we employ ray tracing simulations with the aid of the ray trace OTSun python package [26]. It is a Monte Carlo ray tracing where the optics is implemented through the Fresnel optics equations in their most general form, complemented by the transfer-matrix method (TMM) to account for the interference phenomenon [27, 28]. This software allows us to perform the simulations by loading a geometry file designed with the aid of FreeCAD [29], an open-source software for the parametric modeling of geometric figures in 3D. The simulations require knowledge of the layer thicknesses as well as the complex refractive indexes of the corresponding materials as a function of wavelength (λ). In particular, the complex refractive indexes of the following materials have been taken from literature: FTO [41], TiO_2 [42], Spiro-OMeTAD [43]. In the case of SnO_2 and SiO_2 the data are taken from the material manufacturer itself. According to the experimental setup [24] the chemical structure of the perovskite layer has been associated with FaPbI_3 . In this case the complex refractive index data are taken from [34], where the real and imaginary parts of the refractive index have been measured for a similar perovskite. The physical characteristics of all layers that form the architecture of our device are displayed in Table I.

On the other hand, if the layer contains a few constituents there is a need in some effective approach. The refractive index of the glass has been calculated from transmittance experimental measurements, while for the mp- TiO_2 material we have developed the effective approach to determine its complex refractive index (see below).

Glass complex refractive index

Since the glass substrate consists of a few thin components, to determine the glass optical properties itself the oxides films have to be removed. To this aim, on the glass multilayer system the etching process is done by using Zn powder and HCl solution. As a result, the optical properties of the glass substrate has been determined with the aid of the method [44], based on the ideas discussed be-

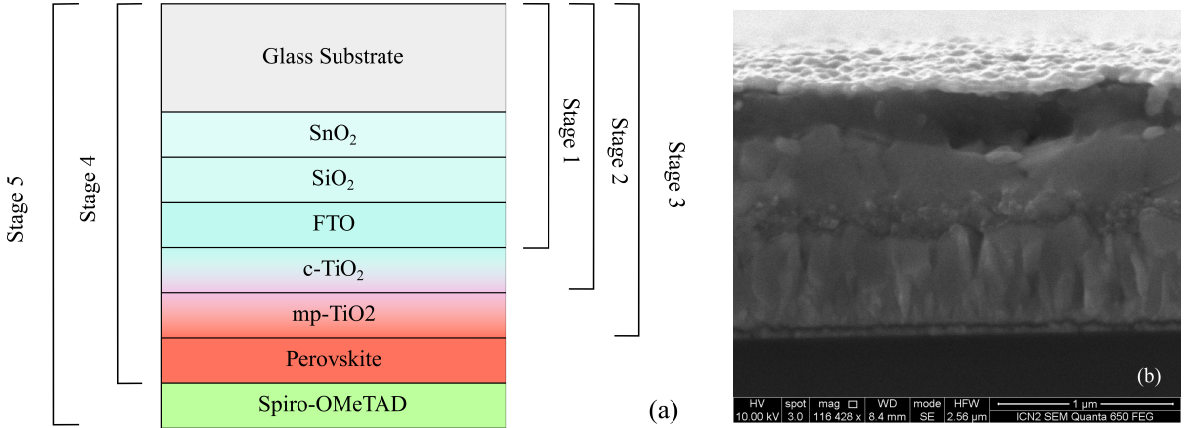


FIG. 1: (a) Structure of the layers present in each manufacturing stage. A total of five stages in which the optical behavior has been studied. (b) Typical cross-section image of the sample, obtained by means of the scanning electron microscope.

Input parameters in our calculations (References)				
	c-TiO ₂	mp-TiO ₂	Perovskite	Spiro-OMeTAD
χ [eV]	4 [30]	4 [30]	3.75 [31]	2.12 [32]
E_g [eV]	3.05 [33]	3.05 [33]	1.66 [34]	3.1 [35]
m_e^*	1	1	1	1
m_h^*	1	1	1	1
$N_{d/a}$ [cm ⁻³]	1×10^{18}	variable	0	1×10^{21}
μ [cm ² /Vs]	0.006 [36]	0.006 [36]	variable	0.0001 [37]
ϵ	60 [38]	42.45**	60 [39]	3 [40]
ℓ_D [nm]	4	4	variable	0.5

TABLE I: Characteristics of the considered semiconductors: TiO₂, FAPbI₃ (Perovskite), Spiro-OMeTAD. We use the following notations: χ is an electron affinity; E_g is an energy gap; $m_{e/h}^*$ is an effective electron/hole mass; $N_{d/a}$ is a donor/acceptor concentration; μ is a mobility; ϵ is a permittivity; ℓ_D is a diffusion length.(**) The definition of the permittivity of the mp-TiO₂ is discussed in Sec.II B; see Eq.10 and the accompanying discussion.

low. If the slab of material has plane-parallel faces, and a material is absorbing partially ($k^2 \ll n$), the real part n and the imaginary part k of the refractive index of the slab can be calculated from the intensity of reflectance $R(\lambda) \equiv R$ and transmittance $T(\lambda) \equiv T$ spectra (for the sake of convenience we omit the symbol λ). In particular, the following analytical formulas have been used:

$$k = \frac{\lambda}{4\pi d} \ln \left[\frac{R_F \cdot T}{R - R_F} \right], \quad (1)$$

$$n = \frac{1 + R_F}{1 - R_F} + \left[\frac{4R_F}{(1 - R_F)^2} - k^2 \right]^{1/2}, \quad (2)$$

where the slab geometrical thickness, d , is assumed as known, and

$$R_F = (2 + T^2 - (1 - R)^2 - \{[2 + T^2 - (1 - R)^2]^2 - 4R(2 - R)\}^{1/2})(2(2 - R))^{-1}. \quad (3)$$

Experimental results for the transmittance $T(\lambda)$ and reflectance $R(\lambda)$ spectra, and the complex refractive index, obtained by means of Eqs.(1)–(3), are shown in Fig.2.

Mesoporous layer as an effective medium: an optical approach

Mesoporous TiO₂ is one of the commonly used electron transport materials (ETMs) in PSCs. The mp-TiO₂

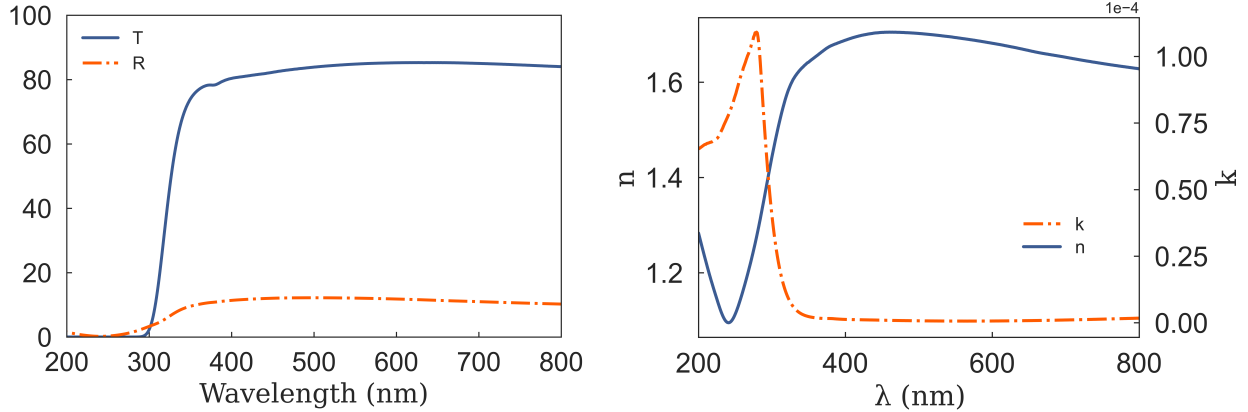


FIG. 2: Left panel: the results of transmittance and reflectance measurements of the glass substrate as a function of the wavelength are shown. Right panel: the real (n) and imaginary (k) components of the calculated complex refractive index of the glass substrate as a function of the wavelength are displayed.

film serves not only as a scaffold for the perovskite layer but also as a route for electron transport. However, in many simulations (see, for example, [45–48]) the effect of the porosity of the mesoporous TiO_2 layer on optical and electronic properties meso-structured perovskite solar cells is ignored.

The presence of mesoporous thin films requires a proper approach to determine its optical characterization. Several effective medium approximations have been suggested to describe the optical properties of heterogeneous thin films by considering them as a homogeneous media with an effective refractive index, along with effective absorption coefficient. Most of the models have been developed for the effective refractive index omitting the absorption coefficient (see for a review [49]). However, the absorption can affect the optoelectronic properties of ETM, and, consequently, the properties of the whole system.

To consider the complex refractive index we apply the Volume Average Theory (VAT) model, discussed among others in [49]. It provides the effective complex refractive index (subindex eff) of a material (see Eqs.(4)–(7)) composed of a continuous phase material matrix (subindex c) and a dispersed phase material matrix (subindex d), with a porosity p :

$$n_{\text{eff}}^2 = \frac{1}{2}(A + \sqrt{A^2 + B^2}) \quad (4)$$

$$k_{\text{eff}}^2 = \frac{1}{2}(-A + \sqrt{A^2 + B^2}) \quad (5)$$

$$A = p(n_d^2 - k_d^2) + (1-p)(n_c^2 - k_c^2) \quad (6)$$

$$B = 2pn_dk_d + 2(1-p)n_ck_c \quad (7)$$

The properties of the mp- TiO_2 material can be characterized using an effective medium that contains a mixture

of the c- TiO_2 material and air, as suggested in [50–52]. In the latter paper, however, the effect of the extinction coefficient k is missing. Evidently, it may play important role, since the absorption in the mp- TiO_2 layer depends on the degree of its porosity. To find thickness configurations that match best the experimental results we developed the special procedure to quantify the minimal deviation of the theoretical estimations from the experimental values for the transmittance and the short-circuit current (see Figs.9, 10 and the accompanying text). Once the above analysis has been completed, to gain much more accurate results on the optical properties of the PSC we use the OTSun python package.

Impact of porosity and Lambertian scattering

The knowledge of the thickness configuration enables to us to simulate the photogeneration rate for its application into the electronic transport equations. For the sake of convenience we recapitulate briefly the basic steps of this procedure (see details in [23]).

According to the Beer-Lambert law for a given absorption coefficient $\alpha(\lambda) = 4\pi k(\lambda)/\lambda$ of a material, the loss of light intensity is a function of the path length ℓ of the light beam through a material:

$$N(\ell, \lambda) = N_0(0, \lambda)e^{-\alpha(\lambda)\ell}. \quad (8)$$

Here, $N_0(0, \lambda)$ is the initial number of photons of the incident ray on a material per unit area, per wavelength, and per unit time (for each time when a ray impacts onto a material according to the path trajectories determined by the ray tracing simulation). With the aid of OTSun and Eq.(8), we calculate the generation rate produced by a single ray

$$G(z) = \int_0^\infty \frac{\alpha(\lambda)N_0(0, \lambda)}{\cos \theta} e^{-\alpha(\lambda)z/\cos \theta} d\lambda, \quad (9)$$

where $z = \ell \cos \theta$ is the depth from a semiconductor surface, and θ is the ray refracted angle. The function $G(z)$ provides the number of electrons per unit volume and per unit time, generated at each point in the device due to the photon absorption. The total function $G(z)$ is the sum of all rays (transmitted or reflected) passed at the point z . As a result, obtained PSC thickness configuration and the rate function $G(z)$ allow to calculate the J-V characteristics by means of the transport model [23]. In this model there is a set of parameters that are relatively well established either from literature or from measurements. Besides, there is another set that consists of some uncertain parameters. All of them are listed in Table I, where uncertain parameters are named as “variable”. The latter ones are treated as fitting parameters to explain the measured data.

There are a few comments in order, however. At this stage we have to elaborate the model [23], taking into account the presence of the mp-TiO₂ layer. Consequently, to carry out the calculations within the transport model we have to define the permittivity and the conductivity of the mp-TiO₂ layer $\sigma_{mp} = q\mu_{mp}N_{mp}$; here μ_{mp} is a majority carriers mobility, and N_{mp} is the doping concentration.

From the optical properties of different layers, we obtain the fact that the mp-TiO₂ layer includes air-filled holes (porosity). As the concentration of these holes is small ($\sim 20\%$), we apply the electrodynamic approach developed for weakly mixed systems (see the textbook [53]). In this case the permittivity of the mp-TiO₂ material is provided by the expression for permittivity of the mixture ε_{mix} :

$$\varepsilon_{mix} = \varepsilon_{TiO_2} + c \frac{3(\varepsilon_a - \varepsilon_{TiO_2})\varepsilon_{TiO_2}}{\varepsilon_a + 2\varepsilon_{TiO_2}}, \quad (10)$$

where ε_{TiO_2} and ε_a are the permittivities of TiO₂ and air, respectively; c is the concentration of holes. As for the conductivity, we make use of the fact obtained from the optical properties fitting. Due to small concentration of air-filled holes in the mp-TiO₂ layer one can suppose that the conductivity in this layer should be reduced on 20% as well. As a result, it seems reasonable to assume that for the donor concentration holds the relation $N_{mp} = 0.8 \cdot N_c$, while the mobility of the carriers remains the same $\mu_{mp} = \mu_c$, as in the c-TiO₂ layer (see Sec.III). To obtain the better agreement with the J-V characteristics of our experimental device, we propose to vary only the unknown parameters N_{mp} , the mobility of carriers μ and their relaxation time τ in the perovskite layer, keeping the other parameters fixed.

It is important to stress that OTSun provides a more accurate form of the photogeneration rate $G(z)$ compare to the TMM approach used in Appendix A, since non-specular reflection and multiple reflection are considered. In particular, from images obtained with the aid of the scanning electron microscope (see Fig.8) it can be seen that the gold layer (the top layer) has nano-sized roughness, of the order of magnitude of its thickness (~ 80

nm). With a high degree of certainty, it can be argued that these textures provide a Lambertian reflection to the surface. Such textures randomly reflect the light that impacts on the gold layer, and, consequently, increase the optical path in the perovskite, and the photocurrent (cf.[11]). As a result, taking into account all facts above, we obtain by means of Eq.(9) that $J_{sc} = 20.15 \text{ mA/cm}^2$ (see Fig.10), i.e., it is slightly higher than the TMM result and closer to the experimental value.

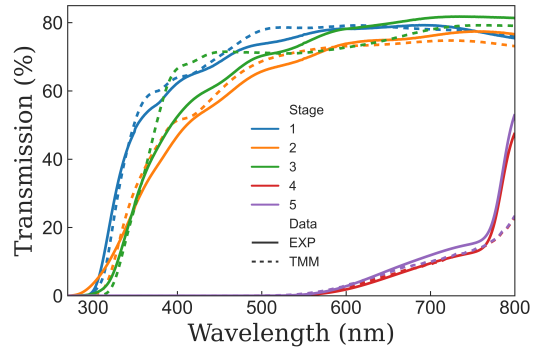


FIG. 3: Experimental (solid line) and theoretical (dotted line) transmittance curves for the different manufacturing stages of the PSCs under study. For the stage identifications see also Fig.1

III. RESULTS AND DISCUSSION

Begin with, we recall the main result on the analysis of the layer thicknesses (see details in Appendix A). The layer configuration chosen as the theoretical model of the PSCs studied is (in nm): 11 (SiO₂), 16 (SnO₂), 565 (FTO), 24 (c-TiO₂), 240 (mp-TiO₂, porosity = 20%), 500 (Perovskite), 250 (Spiro-OMeTAD). The result of this final disposition that produces the best consistency between theoretical and experimental values for the short-circuit current and the optical transmittance in each stage of the manufacturing process is displayed in Fig.3.

There is a rather well agreement between experimental and theoretical results, except two cases: stage 3 and stage 4. The visible difference between the experimental and theoretical curves is located in the wavelength region 380 – 500 nm. This result implies some inaccuracy in estimation of the mp-TiO₂ layer absorption coefficient. Theoretical result exhibits the larger absorption for the perovskite FAPbI₃ (stage 4) in comparison with that of the experimental sample in the wavelength range 770 – 800 nm. This disagreement is due to the difference between the experimental value of the perovskite absorption coefficient and that adopted from [34]. Since this difference is located at a small interval 760 < λ < 800 nm of the right boundary of the considered wavelength region, it may be safely ignored in the description of the J-V characteristics discussed below.

The values of theoretical layer thicknesses and material parameters (see Table I) are used as the input parameters in the electronic transport model to fit the simulated and measured J-V characteristics of the PSC. The fitting procedure is described in [23] but here we mention some peculiarities:

- 1 The main source of difference between the simulated and the measured short-circuit current has been related in [23] to the reflection properties of the PSC layers. In present paper the reflection properties are already taken into account by our optical model. It results in the remarkable accord between theoretical and experimental values of the short-circuit current (see below).

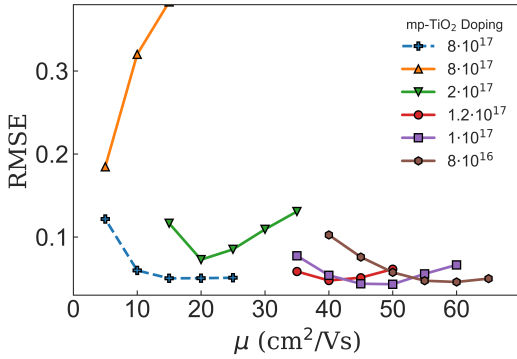


FIG. 4: RMSE as a function of carrier mobility in perovskite for different doping concentration in the mp-TiO₂ layer. The solid curves are associated with the results of calculations without any additional resistances. The dotted line is associated with the results obtained by means of the additional resistances (see details in the text).

- 2 To fit the simulated and “measured averaged” open circuit voltage (V_{oc}) one needs to vary the carrier lifetimes (τ) in the perovskite [23]. Once we vary the donor concentration N_{mp} and the mobility μ , it is required to fit a τ -value to reproduce the experimental value of V_{oc} . To control the accuracy of the fitting procedure of J-V characteristics, we introduce the root mean square error

$$RMSE = \frac{1}{N} \sqrt{\sum_i [J_{sc}^{exp}(V_i) - J_{sc}^{th}(V_i)]^2}, \quad (11)$$

where the number of steps N is defined by the voltage range interval $V = 0 - V_{oc}$ passed with a step size ΔV . At each new value of the voltage $V_i = i \cdot \Delta V$, we solve the system of nonlinear transport equations (see Sec.2.4 in [23]) to calculate the current and compare its value with the experimental data. The results of calculations manifest the dependence of the RMSE on values of N_{mp} and the mobility μ (see Fig.4).

We recall that the analysis of the transmittance resulted in a degree of porosity of the order of 20% for the mp-TiO₂ layer. Evidently, the presence of the porosity in the mp-TiO₂ layer should affect the donor concentration in this material in comparison to that in the c-TiO₂ layer, which is $1 \cdot 10^{18} \text{ cm}^{-3}$ (see Table I). Consequently, it is natural to suppose that the donor concentration in the mp-TiO₂ layer will decrease to the value $8 \cdot 10^{17} \text{ cm}^{-3}$, proportionally to the degree of its porosity. Taking into account that the porosity affects the permittivity (see Eq.10) and the donor concentration of the mp-TiO₂ layer, we solve the transport equations and reach the RMSE minimum (0.18 mA/cm^2) at $\mu = 5 \text{ cm}^2/(\text{V}\cdot\text{s})$ (see Fig.4; triangles connected by solid yellow line). There is a visible difference between the simulated and the “measured averaged” J-V characteristics (see Fig.5(a)).

A fairly common trick in the calculation of J-V characteristics is to use the analogy of the PSC to a current generator in parallel with a diode (see, for example, the analysis in [11]). Hereafter we follow this procedure, since such an approach enables us to consider the parasitic resistance of the contacts and feeding conductors, R ; the leakage resistance, related to the local short-circuit of electron/hole transport material layers, R_{sh} (see the insert in Fig.5(a)).

Once all necessary additional resistances are generated, we obtain a good agreement of our results with the experimental J-V characteristics. This agreement (see Fig.5(a)) is reached with the aid of the following values of the variable parameters: $\mu=15 \text{ cm}^2/(\text{V}\cdot\text{s})$ (see Fig.4); $R=4 \text{ Ohm}\cdot\text{cm}^2$; $R_{sh} \rightarrow \infty$; $\tau = 2.47 \text{ ns}$ that yields the diffusion length $\ell_D = \sqrt{\mu k_B T \tau / |e|} = 0.3 \mu\text{m}$.

It turns out, however, that we can obtain even better agreement varying the donor concentration in the mp-TiO₂ layer. The variation of the RMSE between simulated and “measured averaged” J-V characteristics yields the RMSE absolute minimum (see Fig.4) at the “optimal” mobility $\mu=50 \text{ cm}^2/(\text{V}\cdot\text{s})$, and the donor concentration $N_{mp} = 1 \cdot 10^{17} \text{ cm}^{-3}$. The optimal carrier lifetimes $\tau=0.7 \text{ ns}$ yields again the diffusion length $\ell_D = 0.3 \mu\text{m}$. At these parameters we obtain a remarkable agreement between the simulated and the “measured averaged” J-V characteristics, without any additional resistances (see Fig.5(b)). It seems that in the mp-TiO₂ layer pore holes generate all necessary additional resistance in the measured device. Consequently, it appears that in the real device the pore dimension occupying 20% of the mp-TiO₂ layer is sufficient to affect optical properties of the PSC. It turns out, however, that only small part of the remaining TiO₂ take part in the conductance due to large amount of defects on the pore boundaries.

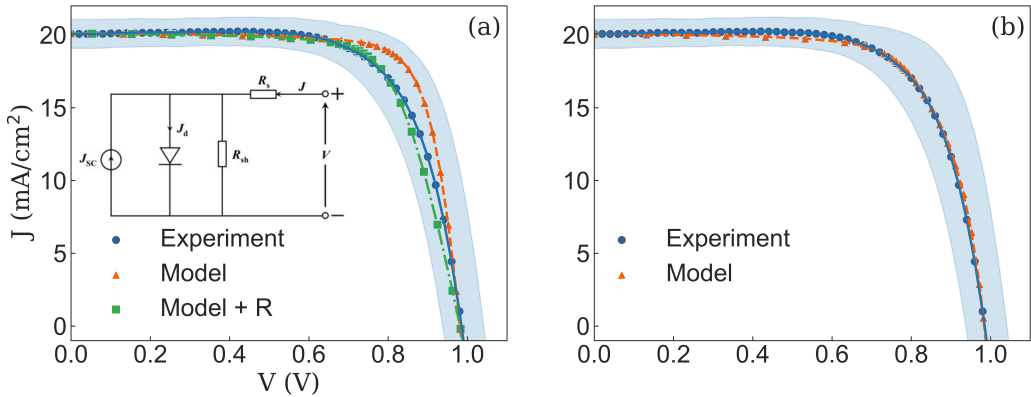


FIG. 5: J-V characteristics. In panels (a) and (b) solid line connecting solid circles is associated with the “measured averaged” values. The panel (a): dashed (dot-dashed) line connecting solid triangles (squares) is associated with the results obtained without (with) additional resistances at 20% porosity of mp-TiO₂ layer. The panel (b): dashed line connecting solid triangles is associated with the results obtained without additional resistances (see for details the text). Light blue band around all these curves marks the range in which the measured J-V characteristics of different samples lie. The insert in the panel (a) displays the circuit layout of the generator.

It is noteworthy, the parameters values obtained by means of our fitting procedure are located within the parameter range considered in literature. In particular, several studies suggest that the doping values of the mp-TiO₂ material are in the range of 10¹⁶ to 10¹⁹ (cm⁻³) [54]. Moreover, the carrier mobility range measured for perovskite is in the range from 5 to 50 (cm²/(V·s))[55]. The degree of the accuracy of our analysis is summarized in Tables II,III. It demonstrates that the short-circuit current, the open circuit voltage, the fill factor and the power conversion efficiency for both simulated and experimental PSC are in a remarkable agreement.

	J_{sc} (mA/cm ²)	V_{oc} (V)	FF	PCE(%)
Experiment	20.072	0.985	0.695	13.735
Model (a)	20.120	0.981	0.772	15.233
Model (a) + R	20.101	0.981	0.705	13.903
Model (b)	20.076	0.984	0.703	13.882

TABLE II: Main PSC parameters for the “measured averaged” device and simulated results obtained by means of our approach. Model (a) is associated with results displayed on the the panel Fig.5(a), without any resistance; the corresponding parameters are presented in the first column of Table III. Model (a) + R is associated with results displayed on the the panel Fig.5(a), with resistance; the corresponding parameters are presented in the second column of Table III. Model (b) is associated with results displayed on the the panel Fig.5(b); the corresponding parameters are presented in the third column of Table III.

Parameters	Model (a)	Model (a) + R	Model (b)
N_{mp} (cm ⁻³)	$8 \cdot 10^{17}$	$8 \cdot 10^{17}$	$1 \cdot 10^{17}$
μ (cm ² /(V·s))	15	15	50
τ (ns)	2.47	2.47	0.7
R (Ohm·cm ²)	—	4	—
R_{sh} (Ohm·cm ²)	—	∞	—

TABLE III: Summary of the parameters used to represent Fig.5 and Table II.

IV. CONCLUSIONS

In summary we have successfully utilized the optoelectronic model based on experimentally obtained optical features for planar meso-structured perovskite solar cells. Our optoelectronic model incorporates ray tracing simulations, the transfer-matrix method and the carrier transport equations. The ray tracing allows the exploration of any geometry, since the solar collector device is designed by means of the FreeCAD software. The combination of the ray tracing with the transfer-matrix method allows to perform the optical simulations considering Fresnel optics, internal reflections of the multilayer system, scattering produced by nanoroughness layers, and effective layers with some peculiarities (such as porous materials).

Large number of transmittance-reflectance measurements on the several stages of manufacturing process have been used to fix the uncertainties of the PSC layers thicknesses and the mesoporous TiO₂ layer porosity. The same number of measurements have been done to define the average J-V characteristics of experimental devices. The obtained results within the optoelectronic model have been further used to analyse J-V characteris-

tics of the manufactured PSCs by means of the optimization procedure based on the multiple-use of the solution transport equations [23]. The developed model demonstrates good agreement with both optical and electrical measurements leading to extraction of the layers thicknesses, the porosity degree and the permittivity of the mesoporous TiO_2 material, the perovskite carriers mobility and lifetimes. In addition, we have found that even small degree of the porosity can affect the performance of the experimental devices, reducing essentially the effective donor concentration (i.e., the conductance) of the mp- TiO_2 layer in comparison to that in the c- TiO_2 layer.

Our approach allows the study of devices with different architectures. Reversing the order of the materials in the solar cell structure does not affect the development of the optoelectronic simulations. Thus our work provides a useful platform for device optimization towards increasing PCE as well as appropriate tools for the analysis of various optoelectronic properties of meso-structured perovskite solar cells.

ACKNOWLEDGEMENTS

This work is part of the project TED2021-132758B-I00, funded by MCIN/ AEI /10.13039/501100011033/ and the European Union “Next Generation EU”/PRTR. It has also been co-funded by the predoctoral contracts call of the Vice-presidency and Innovation, Research and Tourism Department of the Government of the Balearic Islands and the European Social Fund (ESF) [Grant FPI/2144/2018]. Part of this work is under Physics Ph.D. programme for F. Bonnín-Ripoll of the Universitat de les Illes Balears (UIB, Spain). We thank Dr José F. González Morey (Serveis Científicotècnics, UIB) for his technical assistance. This work is partially supported by the Russian Science Foundation (grant no. 23-19-00884). We thank the Spanish State Research Agency for the grant Self-Power (PID2019-104272RB-C54 / AEI / 10.13039/501100011033), the ProperPhotoMile Project (PCI2020-112185) and the OrgEnergy Excellence Network (CTQ2016-81911- REDT), and to the Agència de Gestió d’Ajuts Universitaris i de Recerca (AGAUR) for the support to the consolidated Catalonia research group 2021 SGR 01617 and the Xarxa d’R+D+I Energy for Society (XRE4S). Part of this work is under Materials Science Ph.D. Degree for K.T. and the Chemistry Ph.D. programme for C.P. of the Universitat Autònoma de Barcelona (UAB, Spain). ICN2 is supported by the Severo Ochoa program from Spanish MINECO (grant no. SEV-2017-0706) and is funded by the CERCA Programme/Generalitat de Catalunya.”

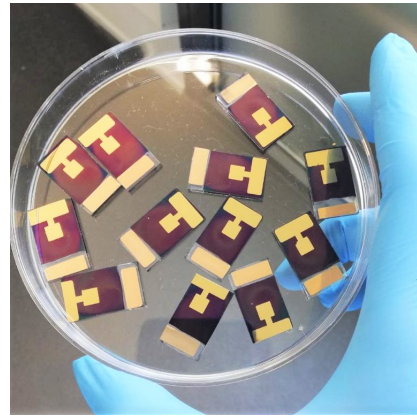


FIG. 6: Image of the perovskite solar cell samples at the final stage of the manufacturing process.

Appendix A: Supplementary data

Device Characteristics

The device fabrication and the experimental work, presented in this paper, have been carried out at the facilities of the Institut Català de Nanociència i Nanotecnologia (ICN2) in collaboration with the Nanomaterials for Photovoltaics Energy research group. The perovskite solar cells have been fabricated with the FTO/c- TiO_2 /mp- TiO_2 /Perovskite/Spiro-OMeTAD/Au configuration using multi-cationic perovskite. Each of these materials has its own synthesis and deposition process; all fabrication details are discussed in [24]. Example of final samples is shown in Fig.6.

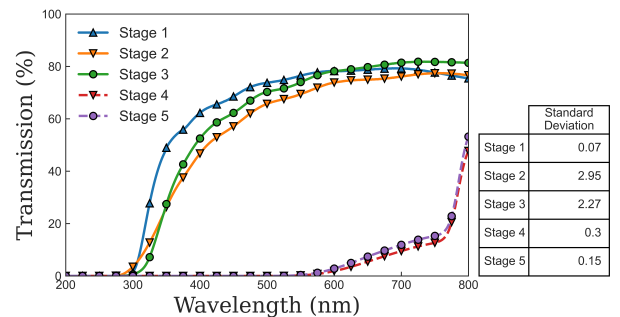


FIG. 7: Mean values and standard deviations of the optical transmittance measurements for each manufacturing stages of the perovskite solar cell. Standard deviations have been calculated at each wavelength for six experimental samples (see also the main text).

Transmittance

Transmittance measurements have been done by means of the UV-Vis CARY 4000 spectrophotometer at normal incidence, using the solid sample holder accessory. The incident radiation consists of 200 – 800 nm wavelength range of the optical spectrum. The results of the mean value of the optical transmittance measurements for each stage as a function of the wavelength are shown in Fig.7. Our measurements make manifest that it is enough to fabricate six samples at each stage to obtain a reliable result for the mean value. Additionally, we indicate the standard deviation from the mean value for each curve, corresponding to each stage. The largest deviations are obtained for the c-TiO₂ and mp-TiO₂ depositions (stages 2 and 3, respectively). Noteworthy, up to now there is no any available criterium in literature regarding definition of the effective border line between c-TiO₂ and mp-TiO₂ depositions. In fact, one of our goals is to propose such the effective methodology.

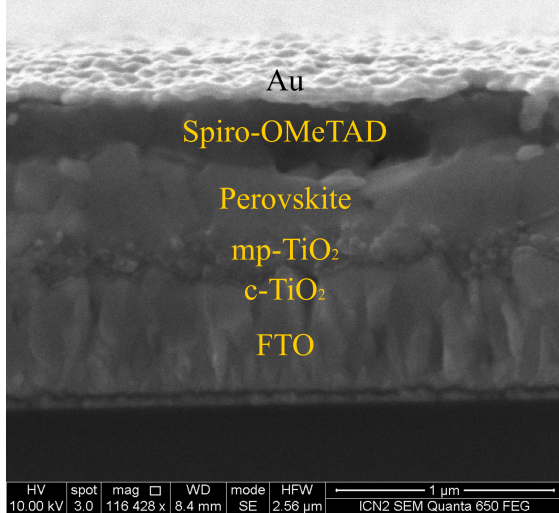


FIG. 8: Cross-section image of the samples, obtained by means of the scanning electron microscope. It is quite visible the degree of the gold layer roughness. The extracted approximate thickness of each layer is presented in Table IV.

Layer Thicknesses

The approximate thickness of each material layers has been estimated using scanning electron microscopy (SEM) techniques (see Fig.8). These images are essential for modelling the PSC, since each layer thickness assessment is a key parameter in the following model calculations. The heterogeneity observed in the layer thicknesses is due to the experimental process itself, subject to variations in the initial conditions, the experience and skill of the technician, the correct stoichiometric balance of

the compounds, etc. The less accuracy for the estimation of the c-TiO₂ layer thickness is due to its extension diapason in the range of a few tens of nanometers.

Material	Thicknesses (nm)
SiO ₂	10-30
SnO ₂	10-30
FTO	500-600
c-TiO ₂	10-30
mp-TiO ₂	180-300
Perovskite	400-550
Spiro-OMeTAD	200-250

TABLE IV: Thickness range of the material layers present in the PSC samples measured by scanning electron microscopy.

Note that the substrate is formed by four different materials. The thickness of each component in the compound is provided by the manufacturer itself: 2.2 mm of glass, 25 nm of SnO₂ and SiO₂, and 540 nm of FTO. Even so, in the images (see Fig.8) it can be seen that the FTO is not completely homogeneous. Consequently, we consider a certain range of thicknesses, in which the calculations for the characterization are carried out. From the images obtained by SEM, the thickness ranges considered for the materials in the successive calculations, are shown in Table IV.

Detailed elaboration of thickness configuration

In order to fit theoretical and experimental transmittances, a concrete thickness configuration of the PSC structure is needed. Since scanning electronic microscope images show that the thicknesses of the layers is not completely homogeneous, we must consider a range between which each layer thickness lies. Before to resolve this problem we have to analyse the optical properties of each layer.

One of the most common theoretical tools used to analyse the optical properties of complex solar systems with a high accuracy is the so called Monte-Carlo ray tracing simulation. It consists of a set of techniques that determine the path of light through matter in a three-dimensional environment with computer simulations [56]. We implement in our approach the Monte-Carlo ray tracing technique, adding the transfer-matrix method (TMM) to characterize the optical response of the PSC with the aid of the ray trace OTSun python package [57–59]. In order to carry out simulations in a simpler and faster way, first, we use the TMM only to determine the thicknesses configuration. Based on the results discussed hereafter, the OTSun will be used (see the main text) as the subsequent step where more accurate calculations are needed. Consequently, using the ranges shown in Table IV, each possible configuration is

considered to provide the transmittance with the aid of the TMM calculation, to obtain those that are closer to the experimental curves. To reach our goal we introduce the root mean square error (RMSE) of each thickness configuration for a given material thickness

$$RMSE = \frac{1}{N} \sqrt{\sum_{\lambda=300}^{\lambda=800} [T^{exp}(\lambda) - T^{th}(\lambda)]^2}. \quad (A1)$$

Here, N is the total number of wavelength steps; the step is equal to 1 nm in all cases; $T^{exp}(T^{th})$ is the experimental (theoretical) optical transmittance. Hereafter, it is convenient to introduce the range limits of the thickness variation for each layer as $[a,b]$ (in nm).

First, we carry out the calculations for the stage 1. To this aim we consider the following thicknesses: [10,30] for SnO_2 and SiO_2 ; [500, 600] for FTO. As a result, we choose those configurations that lie within 1% of the lowest RMSE.

Next, we proceed to the stage 2 (repeating similar calculations), using the range limits obtained from the stage 1: [10,20] for SnO_2 and SiO_2 ; [550,600] for FTO; [10,30] for c-TiO₂. These calculations reduce the starting range limits to [10,16], [14,20], [550,600], [22,30] for SnO_2 , SiO_2 , FTO, c-TiO₂, respectively.

Afterwards, we move to the stage 3, where both the thickness and the porosity of the mp-TiO₂ are added to the system. An initial sweep is made considering the previous ranges plus the mp-TiO₂ [180,300] layer and its porosity considered between 1% and 50%. Considering the configurations that lie within 1% of the lowest RMSE, the material thicknesses are varied in the following intervals: [10,12] for SnO_2 ; [14,18] for SiO_2 ; [555,580] for FTO; [23,25] for c-TiO₂; [200,300] for mp-TiO₂, and its porosity reduced to the 10%–20% range.

From our previous experience (see details in [11, 23]) it follows that small changes in layer thicknesses (in order of a few nanometers) at the stage 2 do not affect the optical transmittance of the device. Therefore, we choose the mean values 11, 16, 565, and 24 nm (associated with SnO_2 , SiO_2 , FTO, c-TiO₂ layer thickness, respectively), which are defined within the ranges imposed by the stage 3. By fixing these values, we also reduce significantly the calculation time, enabling us to explore the mesoporous material and its subsequent influence on the properties of the absorbing layer.

We recall that the stage 4 includes the perovskite layer considered in the [400,550] interval, while keeping the variability of the porosity and thickness of the mp-TiO₂ layer as mentioned above. Since there is a complex interplay of the transmittance through the mp-TiO₂ layer and its effect on the transmittance through the perovskite, we consider the ranges of three parameters simultaneously: i) the mp-TiO₂ layer thickness; ii) its porosity; iii) the perovskite thickness within 5% of the lowest RMSE selection. As a result, we obtain that: the mp-TiO₂ porosity oscillates between 10% and 20%, while its thickness

between 260 and 300 nm; the perovskite layer thickness oscillates between 450 and 500 nm. In the stage 5 the Spiro-OMeTAD layer is added with a thickness defined in [200,250] nm interval. Our calculations yield that the configurations within 5% of the lowest RMSE lie in the following interval (in nm): [270,300] for the mp-TiO₂ layer; the porosity is defined between 15% and 20%; [450,470] for the perovskite layer; [200, 250] for the Spiro-OMeTAD layer.

Notice that the configurations that fit better the optical behaviour of the experimental samples are not necessarily those that fit better the electronic properties of the experimental samples. Consequently, our analysis is supplemented by one more parameter: the short-circuit current J_{sc} . Therefore, considering the ranges of parameters for each material obtained under the previous procedure and making them less restrictive, we proceed to the calculations of the short-circuit current J_{sc} , which will involve adding the gold metal layer to the system. Again, we have to vary the discussed parameters within the above limits (see below). Taking this fact into account, the maximum possible photocurrent is calculated in the assumption that all absorbed photons generate electron and holes and contribute to the current [40]. In an efficient PSC this current is closely related to the short-circuit current, J_{sc} . As a result, to reach a consistently between optical and electronic properties we calculate the short-circuit current for every configuration, taking into account that the mean value of the measured current $J_{sc} = 20.07 \text{ mA/cm}^2$ (see details in the main text).

We recall that all the effects regarding the radiation-matter interaction mentioned above, are needed to elucidate the number of absorbed photons inside active materials. To this aim the photogeneration rate G of the creation of pairs of electrons/holes should be considered a position-dependent function within the material thickness. To this aim we employ the method proposed by Ball et al. [60] and the TMM library [27] to calculate the short-circuit current J_{sc} as:

$$J_{sc} = q \int G(\lambda, z) d\lambda dz, \quad (A2)$$

where q is the electron charge, and z is the depth from the semiconductor surface. Turning to the calculation details of the discussed procedure, first, we fix the multilayer glass thicknesses at 11, 16, 565 (nm) for SnO_2 , SiO_2 , FTO, respectively; and 24 nm for c-TiO₂. Second, it is observed that the photocurrent is very sensitive to the thickness and porosity of the mp-TiO₂ layer. Indeed, it should be noted that at stages 2 and 3 that correspond to the deposition of the c-TiO₂ and the mp-TiO₂ layers, respectively, a standard deviation 10 times higher relative to those for other stages (see Fig.7). Including the J_{sc} calculations to the RMSE result obtained from the transmittance fitting, we weaken the boundaries found above, in particularly, for the porosity and for the mp-TiO₂ layer thickness. Consequently, we vary the porosity

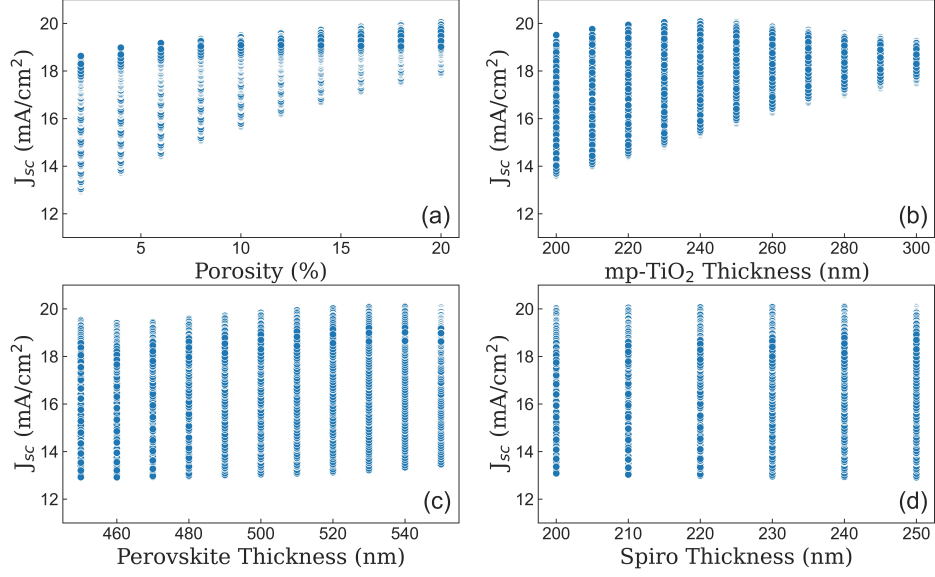


FIG. 9: The short-circuit current J_{sc} as a function of mp-TiO₂ porosity (a), mp-TiO₂ thickness (b), perovskite thickness (c) and Spiro-OMeTAD thickness (d).

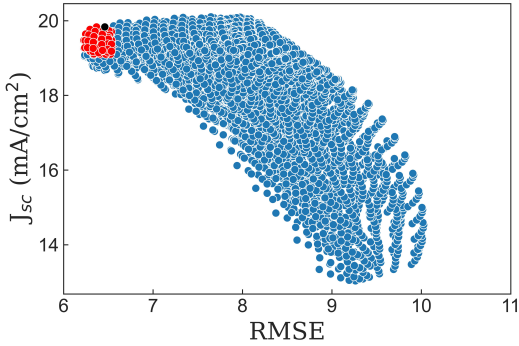


FIG. 10: The short-circuit J_{sc} as a function of the RMSE, calculated by fitting the experimental and theoretical transmittance of stage 5. The optimal configurations (red solid points) are located in the range of $\pm 5\%$ deviation from the experimental value of the short-circuit current. Black point corresponds to the selected case, used for comparison of experimental and theoretical J-V characteristics (see main text).

and thickness of the mp-TiO₂ layer (from 2% to 20%, from 200 to 300 nm, respectively); the perovskite thickness (from 450 to 550 nm); the Spiro-OMeTAD thickness (from 200 to 250 nm). As a result, we do calculations by varying the following parameters:

1 porosity takes 10 possible values;

2 mp-TiO₂ thickness takes 11 possible values;

3 perovskite thickness takes 11 possible values;

4 Spiro-OMeTAD thickness takes 6 possible values, i.e. we have a set of $10 \times 11 \times 11 \times 6 = 7260$ combinations determined by the parameters variations. Altogether the chosen parameters provide the basis for the calculation of the set J_{sc} values (see Fig.9).

Among all the possible configurations, we have selected those that hold the following criteria: i) be $\leq |5\%|$ with respect to the experimental value of the short-circuit current J_{sc} ; ii) be $\leq 5\%$ of the lowest RMSE (red region in Fig.10). From this selection, the configuration with the highest J_{sc} has been chosen denoted by the black point on Fig.10. The results for the short-circuit current J_{sc} demonstrate: i) its less sensitivity to the variation of the perovskite and Spiro-OMeTAD thicknesses; ii) while the close correspondence to the experimental value of the short-circuit current J_{sc} takes place at the thickness 240 nm and the porosity value = 20% of the mp-TiO₂ layer.

Summarising, according to our analysis the theoretical configuration, chosen to model the experimental samples, consists of the following layer thicknesses (in nm): 11 (SiO₂), 16 (SnO₂), 565 (FTO), 24 (c-TiO₂), 240 (mp-TiO₂, the porosity = 20%), 500 (Perovskite), 250 (Spiro-OMeTAD). This configuration is obtained as a result of optimization of the optical transmittance of the device configuration at the value of the short-circuit current $J_{sc} = 19.83 \text{ mA/cm}^2$.

[1] H. Min, D. Y. Lee, J. Kim, G. Kim, K. S. Lee, J. Kim, M. J. Paik, Y. K. Kim, K. S. Kim, M. G. Kim, T. J. Shin,

and S. Il Seok, Nature 2021 598:7881 **598**, 444 (2021).

- [2] V. Babu, R. Fuentes Pineda, T. Ahmad, A. O. Alvarez, L. A. Castriotta, A. Di Carlo, F. Fabregat-Santiago, and K. Wojciechowski, *ACS Applied Energy Materials* **3**, 5126 (2020).
- [3] Y. B. Martynov, R. G. Nazmitdinov, A. Moià-Pol, P. P. Gladyshev, A. R. Tameev, A. V. Vannikov, and M. Pudlak, *Phys. Chem. Chem. Phys.* **19**, 19916 (2017).
- [4] R. Urzúa-Leiva, A. Narymany Shandy, H. Xie, M. Lira-Cantú, and G. Cárdenas-Jirón, *New journal of chemistry* **44**, 14642 (2020).
- [5] A. Frontera, Y. Martynov, R. G. Nazmitdinov, and A. Moià-Pol, in *Perovskite Solar Cells: Properties, application and efficiency* (Nova Science Publishers/ Inc., 2019) Chap. 3, pp. 117–174.
- [6] A. Agresti, A. Pazniak, S. Pescetelli, A. Di Vito, D. Rossi, A. Pecchia, M. Auf der Maur, A. Liedl, R. Larciprete, D. V. Kuznetsov, D. Saranin, and A. Di Carlo, *Nat. Mater.* **18**, 1228 (2019).
- [7] Y. B. Martynov, R. G. Nazmitdinov, P. P. Gladyshev, and A. Moià-Pol, *Mendeleev Communications* **31**, 459 (2021).
- [8] T. Li, S. Wang, J. Yang, X. Pu, B. Gao, Z. He, Q. Cao, J. Han, and X. Li, *Nano Energy* **82**, 10.1016/J.NANOEN.2021.105742 (2021).
- [9] X. Zhang, J. Wu, S. Wang, W. Pan, M. Zhang, X. Wang, Z. Lan, and J. Lin, *ACS Applied Energy Materials* **4**, 10.1021/ACSAEM.1C01142 (2021).
- [10] C. Pereyra, H. Xie, and M. Lira-Cantu, *Journal of Energy Chemistry* **60**, 599 (2021).
- [11] F. Bonnín-Ripoll, Y. B. Martynov, G. Cardona, R. G. Nazmitdinov, and R. Pujol-Nadal, *Solar Energy Materials and Solar Cells* **200**, 110050 (2019).
- [12] K. Deng, L. Li, K. Deng, and L. Li, *Small Methods* 10.1002/smtd.201900150 (2019).
- [13] G. Haidari, *AIP Advances* 10.1063/1.5110495 (2019).
- [14] A. K. Mishra and R. K. Shukla, *Materials Today: Proceedings* **49**, 3181 (2020).
- [15] A. Husainat, W. Ali, P. Cofie, J. Attia, J. Fuller, and A. Darwish, *American Journal of Optics and Photonics* **8**, 6 (2020).
- [16] M. Al-Hattab, L. Moudou, M. Khenfouch, O. Bajjou, Y. Chrifi, and K. Rahmani, *Solar Energy* **227**, 10.1016/J.SOLENER.2021.08.084 (2021).
- [17] S. S. Hussain, S. Riaz, G. A. Nowsherwan, K. Jahangir, A. Raza, M. J. Iqbal, I. Sadiq, S. M. Hussain, and S. Naseem, *Journal of Renewable Energy* **2021**, 10.1155/2021/6668687 (2021).
- [18] R. K. Yadav, P. S. Pawar, R. Nandi, K. R. E. Neerugatti, Y. T. Kim, J. Y. Cho, and J. Heo, *Solar Energy Materials and Solar Cells* **244**, 10.1016/J.SOLMAT.2022.111835 (2022).
- [19] K. Ahmad, M. Q. Khan, R. A. Khan, and H. Kim, *Optical Materials* **128**, 10.1016/J.OPTMAT.2022.112458 (2022).
- [20] S. Karthick, S. Velumani, and J. Bouclé, *Optical Materials* **126**, 10.1016/J.OPTMAT.2022.112250 (2022).
- [21] M. Burgelman, K. Decock, A. Niemegeers, J. Verschraegen, and S. Degrave, *SCAPS-1D Manual* (2021).
- [22] K. Deepthi Jayan and V. Sebastian, *Solar Energy* **217**, 40 (2021).
- [23] F. Bonnín-Ripoll, Y. B. Martynov, R. G. Nazmitdinov, G. Cardona, and R. Pujol-Nadal, *Physical Chemistry Chemical Physics* 10.1039/D1CP03313A (2021).
- [24] H. Xie, Z. Wang, Z. Chen, C. Pereyra, M. Pols, K. Galkowski, M. Anaya, S. Fu, X. Jia, P. Tang, D. J. Kubicki, A. Agarwalla, H. S. Kim, D. Prochowicz, X. Borrisé, M. Bonn, C. Bao, X. Sun, S. M. Zakeeruddin, L. Emssley, J. Arbiol, F. Gao, F. Fu, H. I. Wang, K. J. Tiellooij, S. D. Stranks, S. Tao, M. Grätzel, A. Hagfeldt, and M. Lira-Cantu, *Joule* **5**, 1246 (2021).
- [25] H. Liu, Z. Huang, S. Wei, L. Zheng, L. Xiao, and Q. Gong, *Nanoscale* **8**, 6209 (2016).
- [26] G. Cardona and R. Pujol-Nadal, *PLOS ONE* **15**, e0240735 (2020).
- [27] S. Byrnes, *tmm 0.1.7 : Python Package Index* (2017).
- [28] S. J. Byrnes, *Multilayer optical calculations* (2020), arXiv:1603.02720 [physics.comp-ph].
- [29] FreeCAD: Your Own 3D Parametric Modeler (2001).
- [30] F. Liu, J. Zhu, J. Wei, Y. Li, M. Lv, S. Yang, B. Zhang, J. Yao, and S. Dai, *Appl. Phys. Lett.* **104**, 253508 (2014).
- [31] A. Hima, *Int. J. Energetica* **4**, 56 (2019).
- [32] F. Zhang, Z. Wang, H. Zhu, N. Pellet, J. Luo, C. Yi, X. Liu, H. Liu, S. Wang, X. Li, Y. Xiao, S. M. Zakeeruddin, D. Bi, and M. Grätzel, *Nano Energy* **41**, 469 (2017).
- [33] A. Farhana, R. Mahbub, S. S. Satter, and S. M. Ullah, *Inter. J. Photoenergy* **2017**, 9846310 (2017).
- [34] H. W. Chen, D. P. Gulo, Y. C. Chao, and H. L. Liu, *Scientific Reports* 2019 9:1 **9**, 1 (2019).
- [35] X. Wang, L.-L. Deng, L.-Y. Wang, S.-M. Dai, Z. Xing, X.-X. Zhan, X.-Z. Lu, S.-Y. Xie, R.-B. Huang, and L.-S. Zheng, *J. Mater. Chem. A* **5**, 1706 (2017).
- [36] K. Wojciechowski, M. Saliba, T. Leijtens, A. Abate, and H. J. Snaith, *Energy Environ. Sci.* **7**, 1142 (2014).
- [37] H. J. Snaith and M. Grätzel, *Appl. Phys. Lett.* **89**, 262114 (2006).
- [38] S. Dutta, Leeladhar, A. Pandey, O. P. Thakur, and R. Pal, *J. Vac. Sci. and Tech. A* **33**, 021507 (2015).
- [39] M. Green, A. Ho-Baillie, and H. Snaith, *Nat. Photonics* **8**, 506 (2014).
- [40] J. García-Cañadas, F. Fabregat-Santiago, H. J. Bolink, E. Palomares, G. Garcia-Belmonte, and J. Bisquert, *Synthetic Metals* **156**, 944 (2006).
- [41] E. Ching-Prado, A. Watson, and H. Miranda, *Journal of Materials Science: Materials in Electronics* **29**, 15299 (2018).
- [42] T. Sieffke, S. Kroker, K. Pfeiffer, O. Puffky, K. Dietrich, D. Franta, I. Ohlídal, A. Szeghalmi, E.-B. Kley, and A. Tünnermann, *Advanced Optical Materials* **4**, 1780 (2016).
- [43] C. W. Chen, S. Y. Hsiao, C. Y. Chen, H. W. Kang, Z. Y. Huang, and H. W. Lin, *Journal of Materials Chemistry A* **3**, 9152 (2015).
- [44] E. Nichelatti, *J. Opt. A: Pure Appl. Opt.* **4**, 400 (2002).
- [45] K. P. Kim, W. H. Kim, S. M. Kwon, J. Y. Kim, Y. S. Do, and S. Woo, *Nanomaterials* 2021, Vol. 11, Page 1233 **11**, 10.3390/NANO11051233 (2021).
- [46] E. Widianto, Shobih, E. S. Rosa, K. Triyana, N. M. Nursam, and I. Santoso, *Optical Materials* **121**, 10.1016/J.OPTMAT.2021.111584 (2021).
- [47] M. Mehrabian, O. Akhavan, N. Rabiee, E. N. Afshar, and E. N. Zare, *Environmental Science and Pollution Research* **30**, 10.1007/S11356-023-26497-1/FIGURES/6 (2023).
- [48] M. K. Hossain, G. F. Toki, A. Kuddus, M. H. Rubel, M. M. Hossain, H. Bencherif, M. F. Rahman, M. R. Islam, and M. Mushtaq, *Scientific Reports* 2023 13:1 **13**, 10.1038/s41598-023-28506-2 (2023).
- [49] N. J. Hutchinson, T. Coquil, A. Navid, and L. Pilon,

- Thin Solid Films **518**, 2141 (2010).
- [50] E. Raoult, R. Bodeux, S. Jutteau, S. Rives, A. Yaiche, D. Coutancier, J. Rousset, and S. Collin, in *EU PVSEC Proceedings*, Vol. 36th EU PVSEC 2019 (2019) pp. 757–763.
- [51] E. Raoult, R. Bodeux, S. Jutteau, S. Rives, A. Yaiche, A. Blaizot, D. Coutancier, J. Rousset, and S. Collin, *Optics Express* **30**, 9604 (2022).
- [52] A. Hernández-Granados, A. N. Corpus-Mendoza, P. M. Moreno-Romero, C. A. Rodríguez-Castañeda, J. E. Pascoe-Sussoni, O. A. Castelo-González, E. C. Menchaca-Campos, J. Escoria-García, and H. Hu, *Optical Materials* **88**, 695 (2019).
- [53] L. Landau, E. Lifshitz, and L. Pitaevskii, *Electrodynamics of Continuous Media: Volume 8*, Course of theoretical physics (Elsevier Science, 1995) p. 460.
- [54] M. C. Sellers and E. G. Seebauer, *Thin Solid Films* **519**, 2103 (2011).
- [55] L. M. Herz, *ACS Energy Letters* **2**, 1539 (2017).
- [56] J. Bos-Coenraad, L. Bunthof, and J. Schermer, *Solar Energy* **155**, 1188 (2017).
- [57] G. Cardona and R. Pujol-Nadal, OTSun Python Package (2018).
- [58] OTSunWebApp (2018).
- [59] F. Bonnín-Ripoll, G. Cardona, and R. Nadal-Pujol, Tutorial 2 OTSun Web App (2018).
- [60] J. M. Ball, S. D. Stranks, M. T. Hörantner, Sven Hüttner, Wei Zhang, E. J. W. Crossland, Ivan Ramirez, Moritz Riede, M. B. Johnston, R. H. Friend, and H. J. Snaith, *Energy & Environmental Science* **8**, 602 (2015).